A hybrid discontinuous Galerkin method for tokamak edge plasma simulations in global realistic geometry

Giorgio Giorgiani, Hugo Bufferand, Guido Ciraolo, Philippe Ghendrih, Frédéric Schwander, Eric Serre, Patrick Tamain

▶ **To cite this version:**

Giorgio Giorgiani, Hugo Bufferand, Guido Ciraolo, Philippe Ghendrih, Frédéric Schwander, et al.. A hybrid discontinuous Galerkin method for tokamak edge plasma simulations in global realistic geometry. Journal of Computational Physics, 2018, 374, pp.515-532. 10.1016/j.jcp.2018.07.028 . hal-02114246

HAL Id: hal-02114246
https://amu.hal.science/hal-02114246v1

Submitted on 29 Apr 2019

HAL is a multi-disciplinary open access archive for the deposit and dissemination of scientific research documents, whether they are published or not. The documents may come from teaching and research institutions in France or abroad, or from public or private research centers.

L'archive ouverte pluridisciplinaire **HAL**, est destinée au dépôt et à la diffusion de documents scientifiques de niveau recherche, publiés ou non, émanant des établissements d'enseignement et de recherche français ou étrangers, des laboratoires publics ou privés.

Accepted Manuscript

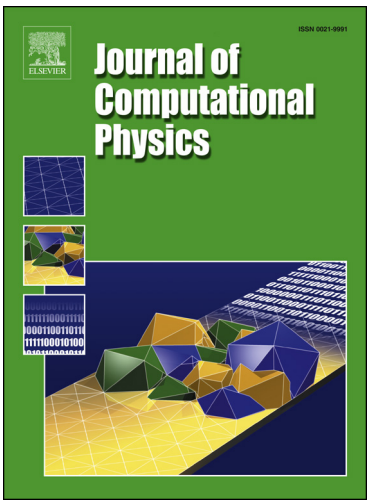

A hybrid discontinuous Galerkin method for tokamak edge plasma simulations in global realistic geometry

G. Giorgiani, H. Bufferand, G. Ciraolo, P. Ghendrih, F. Schwander et al.

PII: S0021-9991(18)30489-3
DOI: https://doi.org/10.1016/j.jcp.2018.07.028
Reference: YJCPH 8153

To appear in: *Journal of Computational Physics*

Received date: 20 September 2017
Revised date: 22 April 2018
Accepted date: 16 July 2018

Please cite this article in press as: G. Giorgiani et al., A hybrid discontinuous Galerkin method for tokamak edge plasma simulations in global realistic geometry, *J. Comput. Phys.* (2018), https://doi.org/10.1016/j.jcp.2018.07.028

This is a PDF file of an unedited manuscript that has been accepted for publication. As a service to our customers we are providing this early version of the manuscript. The manuscript will undergo copyediting, typesetting, and review of the resulting proof before it is published in its final form. Please note that during the production process errors may be discovered which could affect the content, and all legal disclaimers that apply to the journal pertain.

Highlights

- An Hybrid Discontinuous Galerkin solver for fluid equations in edge tokamak plasma.
- The code is carefully verified and validated.
- Potential of such a method to progress towards predictive tools for fusion.

ACCEPTED MANUSCRIPT

A hybrid discontinuous Galerkin method for tokamak edge plasma simulations in global realistic geometry

G. Giorgiani[a,b], H. Bufferand[b], G. Ciraolo[b], P. Ghendrih[b], F. Schwander[a], E. Serre[a,*], P. Tamain[b]

[a] *Aix-Marseille Univ., CNRS, Centrale Marseille, M2P2 Marseille, France*
[b] *CEA, IRFM, F-13108 Saint-Paul-Lez-Durance, France*

Abstract

Progressing toward more accurate and more efficient numerical codes for the simulation of transport and turbulence in the edge plasma of tokamaks, we propose in this work a new hybrid discontinous Galerkin solver. Based on 2D advection-diffusion conservation equations for the ion density and the particle flux in the direction parallel to the magnetic field, the code simulates plasma transport in the poloidal section of tokamaks, including the open field lines of the Scrape-off Layer (SOL) and the closed field lines of the core region. The spatial discretization is based on a high-order hybrid DG scheme on unstructured meshes, which provides an arbitrary high-order accuracy while reducing considerably the number of coupled degrees of freedom with a local condensation process. A discontinuity sensor is employed to identify critical elements and regularize the solution with the introduction of artificial diffusion. Based on a finite-element discretization, not constrained by a flux-aligned mesh, the code is able to describe plasma facing components of any complex shape using Bohm boundary conditions and to simulate the plasma in versatile magnetic equilibria, possibly extended up to the center. Numerical tests using a manufacturated solution show appropriate convergence orders when varying independently the number of elements or the degree of interpolation. Validation is performed by benchmarking the code with the well-referenced edge transport code SOLEDGE2D (Bufferand *et al.* 2013, 2015 [1, 2]) in the WEST geometry. Final numerical experiments show the capacity of the code to deal with low-diffusion solutions.

*Corresponding author
Email address: eric.serre@univ-amu.fr (E. Serre)

ACCEPTED MANUSCRIPT

Keywords: Discontinuous Galerkin, Hybridization, Fusion, Tokamak plasma simulations, Turbulent transport

1. Introduction

Research in magnetic confinement fusion plasmas explores the possibility of producing carbon-free power by using fusion in deuterium-tritium plasmas in machines of toroidal shape known as tokamaks [3]. A critical issue for the fusion operation is to be able to provide the necessary high temperature conditions in the core to sustain burning plasmas while maintaining manageable heat power fluxes on the tokamak wall. The thermal power flows from the core to the wall through a narrow plasma boundary layer, called the Scrape-Off Layer (SOL), where the open magnetic field lines intercept the plasma facing components. The thickness of this boundary layer depends to a large extent on the ratio of the turbulent transport across magnetic field lines to the very rapid transport along them [4].

In this work we are interested in the plasma edge region which encompasses the SOL and the outer part of the closed field region on both sides of the so-called separatrix. The dynamics of the plasma in this region plays a crucial role in the tokamak exhaust system, in plasma refuelling, and in the dynamic of impurities.

~~The high collision frequency of the plasma in this region justifies a fluid approach (see for example in Ref.[5]), that remains standard in the international community.~~

A proper understanding of the edge would require full-f gyrokinetics simulations. Pioneering full-f gyrokinetic simulations of the edge start appearing in the fusion community, addressing physical phenomena of fundamental interest for fusion operation like transport barrier formation [6, 7]. However, despite the exponential growth of computer speed along with significant improvements in computer technology, they remain extremly costly from the computational point of view. It is particularly true in the near-wall region where particle recirculation requires addressing the electron and ion dynamics on the same footing, and in a magnetic topology that is much more complex than in the core. As the consequence fluid approach based on Braginskii equations [8] and drift ordering [9] remains a standard one near the wall where the temperature is lower and the collisional mean free path significantly smaller than in the core.

ACCEPTED MANUSCRIPT

Various 2D and 3D codes already exist in the community, generally based on first and second-order finite-differences / finite-volumes numerical schemes (see a recent review of most of these codes in Refs. [10] and [2]). Two-dimensional transport codes solve axisymmetric averaged fluid equations in the plasma, but are able to take into account surface physics processes and atomic physics in realistic tokamak geometry. However, these codes rely on simple closures involving arbitrary diffusion coefficients to model the average fluxes and stresses due to turbulent fluctuations. Three-dimensional turbulent codes simulate self-consistently all scales of the flow (larger than the grid spacing) but generally in simple geometries and without plasma wall interactions. Consequently, it remains clear today that, despite the constant growth of the computational power, engineering simulations for routine use in ITER size machines and in ITER relevant parameters will be only performed by 2D transport codes providing mean flow solutions.

Progressing towards predictive simulations requires both to progressively enrich the physics included in the models and to continuously improve the accuracy and efficiency of the numerical schemes. On the latter, a certain number of numerical issues have been yet clearly identified that require some new capabilities for the codes :

- Accurately discretize real geometries of tokamak chambers as well as the steep temperature and density gradients occurring in the plasma edge region in order to estimate the right fluxes at the wall.
- Be computationally efficient by reducing the required number of degrees of freedom and by being efficiently parallelizable.
- Be easily extensible to the tokamak center in order to reduce the large number of free parameters by replacing the badly defined inner boundary conditions by fluxes imposed by the physics.
- Be flexible with respect to the magnetic geometry in order to allow variations of the magnetic equilibrium without re-meshing.
- Be easily coupled with the 3D3V Monte Carlo neutral particle transport solver EIRENE [11] based on triangle elements to include the neutrals physics crucial at the edge.

As an attempt to solve all these issues we explore in this work the use of a discontinuous Galerkin (DG) finite-element method to perform tokamak

ACCEPTED MANUSCRIPT

edge plasma simulations in global realistic geometry. The interest in DG methods has increased over the past years. They have proved their suitability to construct robust stabilized high-order numerical schemes on arbitrary unstructured and non-conforming grids in many areas of nonlinear dynamics with high scalability on various types of computer architectures (see some examples in [12]). More precisely, the Hybrid Discontinuous Galerkin HDG method [13, 14, 15, 16, 17, 18, 19, 20, 21, 22] stands out among all DG methods for implicit schemes, thanks to its stability features, ~~its reduced number of degrees of freedom, and~~ its super-convergence property, and its static condensation property allowing us to assemble a global matrix involving unknowns that belong only to the mesh faces (skeleton). Note that in 3D problems, however, where iterative solvers have to be used, static condensation is not enough to ensure the performances of the method since the question of the conditionning of the assembled matrix has to be considered, as recently shown in Ref. [23].

To our knowledge, only few recent works have considered DG methods for problem arising in magnetic confinement fusion. Kinetic simulations have been performed for solving the Vlasov-Poisson system describing the time evolution of a collisionless plasma. The Vlasov equation models the transport of electrons on a uniform background of fixed ions, and it is coupled to the electrostatic potential through Poisson's equation. Heath *et al.* [24] for example propose a coupled Upwind Penalty Galerkin method and show its efficiency by performing accuracy, convergence and conservation tests on a variety of linear and nonlinear problems. Multifluids (ions and electrons) simulations have been also performed. Shumlak *et al.* [25] include electromagnetic effects, and use an unsplit DG method where the hyperbolic fluxes and source terms are integrated simultaneously. 2D and 3D physically relevant simulations are performed on drift turbulence and plasma sheath formation. Michoski *et al.* [26] propose a new parallel DG solver to describe the intermittent turbulent transport of filaments in a simple 2D scrape-off layer with either absorbing or periodic boundary conditions. An interesting development is done in this work on a diffusion/regularization algorithm based on a novel entropy sensor. All these results, benchmarked against theoretical results and other numerical results obtained from well established codes in the community, demonstrate that the DG method is a viable option for integrating conservation laws arising in magnetic fusion plasmas.

The present study aims to evaluate an HDG method for simulating a reduced model of 2D transport equations in realistic tokamak geometry. An

ACCEPTED MANUSCRIPT

outline of the paper is as follows. In Section 2 we present the physical model including the conservation equations together with the boundary conditions and the geometry. As a starting point, we consider here a reduced model of advection diffusion equations for the ion density n and the particle flux Γ in the direction parallel to the magnetic field. This reduced model is of interest because it contains most of the numerical issues met in more complete fluid edge models, i.e. the magnetic geometry complexity, the strong anisotropy between the directions parallel and perpendicular to the magnetic field lines, as well as the wall description through Bohm boundary conditions. In Section 3 we introduce the formulation of the hybrid DG method and in Section 4 the method is verified using manufactured solutions. Finally in Section 5, the simulation of various well-chosen examples show the capacity of this new solver and its potential to address problems of interest regarding transport in the plasma edge of a tokamak with a real geometry.

2. Physical model

We consider flexible 2D magnetic geometries of various complexity mimicking actual tokamaks with limiter or X-point (Figure 1). The equilibrium magnetic field $\mathbf{B}$ is prescribed and encompasses both closed and open flux surfaces. The strong difference of intensity between the poloidal and toroidal components of the magnetic field ($\|\mathbf{B}_p\| << \|\mathbf{B}_t\|$) leads to a privileged flow direction along which the governing equations are projected using differential operators $\boldsymbol{\nabla}_\parallel = \boldsymbol{b} \cdot \boldsymbol{\nabla}$ and $\boldsymbol{\nabla}_\perp = \boldsymbol{\nabla} - \boldsymbol{b}\boldsymbol{\nabla}_\parallel$, where $\boldsymbol{b} = \frac{\mathbf{B}}{\|\mathbf{B}\|}$ is the unitary vector parallel to the magnetic field.

In the drift ordering hypothesis used in this work (see more details in [28, 10]), it is also useful to split the analysis of the dynamics into the parallel and perpendicular directions to the magnetic field, by decomposing the velocity vector $\boldsymbol{u}$ as

$$\boldsymbol{u} = u\boldsymbol{b} + \boldsymbol{u}_\perp. \tag{1}$$

In this decomposition, the perpendicular component of the velocity is analytical, and described in terms of drifts [10]. In this first stage of development, drifts are restricted for simplicity to the ion diamagnetic drift, which is substituted by a curvature drift velocity, $\boldsymbol{u}_{\nabla B}$, to account for the diamagnetic cancellation like in [10]. In dimensional form it writes as:

$$\boldsymbol{u}_{\nabla B} = \frac{2T}{eB}(\boldsymbol{B} \times \boldsymbol{\nabla} B)/B^2. \tag{2}$$

ACCEPTED MANUSCRIPT

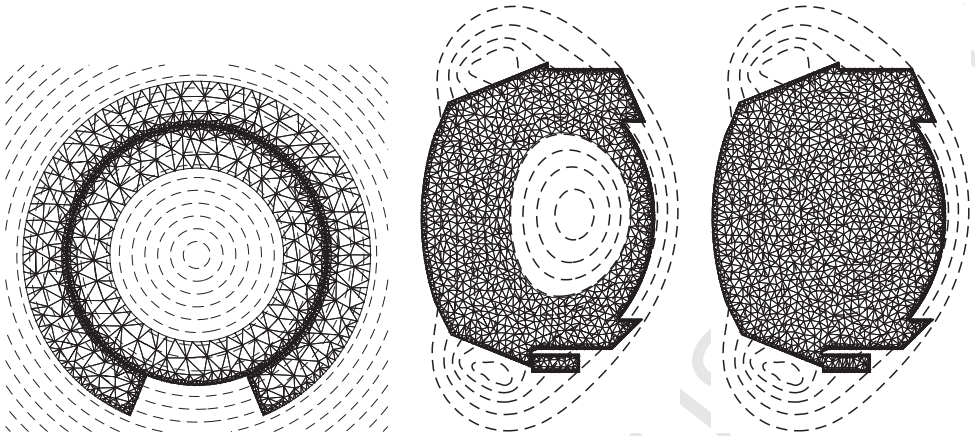

Figure 1: Computational domains and typical unstructured meshes with curved elements. Poloidal circular cross-section with a toroidal limiter (a) and double X-point cross-sections corresponding to WEST [27] (b, c). In (c), the whole cross-section of the tokamak is discretized. Magnetic surfaces are in dashed lines.

This velocity represents the particle guiding center drifts in an inhomogeneous magnetic field.

Two-dimensional fluid conservation equations for electrons and ions can be derived using simplified closures developed by Braginskii [8]. Under some hypothesis and ordering detailed in Refs. [28, 10], a minimum system involving the ion density n and parallel momentum $\Gamma = nu$ can be considered.

Then, in the quasi-neutral limit ($n_e \approx Zn_i$) and neglecting the electron inertia ($m_e/m_i \simeq O(10^{-3})$, m_e and m_i being the mass of the electrons and ions, respectively), the system for an isothermal plasma writes in dimensionless form:

$$\begin{cases} \partial_t n + \boldsymbol{\nabla}\cdot(n\boldsymbol{u}) - \boldsymbol{\nabla}\cdot(D\boldsymbol{\nabla}_\perp n) = S_n, \\ \partial_t \Gamma + \boldsymbol{\nabla}\cdot(\Gamma\boldsymbol{u}) + \boldsymbol{\nabla}_\parallel(c_s^2 n) - \boldsymbol{\nabla}\cdot(\mu\boldsymbol{\nabla}_\perp\Gamma) = S_\Gamma, \end{cases}$$

or using the velocity decomposition with $\boldsymbol{u}_\perp = \boldsymbol{u}_{\nabla B}$:

$$\begin{cases} \partial_t n + \boldsymbol{\nabla}\cdot(\Gamma\boldsymbol{b} + n\boldsymbol{u}_\perp) - \boldsymbol{\nabla}\cdot(D\boldsymbol{\nabla}_\perp n) = S_n, \\ \partial_t \Gamma + \boldsymbol{\nabla}\cdot(\dfrac{\Gamma^2}{n}\boldsymbol{b} + \Gamma\boldsymbol{u}_\perp) + \boldsymbol{\nabla}_\parallel(c_s^2 n) - \boldsymbol{\nabla}\cdot(\mu\boldsymbol{\nabla}_\perp\Gamma) = S_\Gamma, \end{cases} \tag{3}$$

where S_n and S_Γ are two volumetric source terms, possibly included to drive the particle and momentum flux, respectively. The symbol c_s denotes

ACCEPTED MANUSCRIPT

the dimensionless sound speed, while D and μ are two effective diffusions accounting for both collisional transport and turbulence in the cross-field direction (described via a gradient diffusion hypothesis). They are assumed to be constant, and are usually chosen smaller or equal to one. In the present paper they are also assumed to be equal, $D = \mu$.

Remark 1 (Characteristic scales). *A reference temperature $T_0 = 50eV$ and a reference magnetic field $B_0 = 2\,Tesla$ are chosen as characteristic values in the plasma edge. In this isothermal model, the electron and ion temperature T_e and T_i may be given by a steady arbitrary temperature spatial distribution for ions and electrons. In the simulations presented in this paper, the spatial distribution is uniform, $T_i = T_e = T_{bc}$, where T_{bc} defines the background temperature in eV. Time and length are normalized with respect to the ions gyro-motion calculated at these reference values. Thus, the gyro-frequency $\omega_0 = eB_0/m_i$ and the gyro-radius $\rho_L = \sqrt{k_B m_i T_0}/(eB_0)$, where k_B is the Boltzmann constantn e is the electron charge ($e = 1.6 \times 10^{-19}C$) and m_i the ion mass ($m_i = 3.35 \times 10^{-27}kg$) are equal to $9.56 \times 10^7 s^{-1}$ and $0.5mm$, respectively. This also defines a reference velocity, which is used to non-dimensionalize the plasma sound speed $\sqrt{2k_B T_{bc}/m_i}$. Finally, the density is normalized to a reference value n_0.*

Boundary conditions. The system is supplemented here with a simple set of boundary conditions modeling the plasma-wall interaction (more accurate boundary conditions for fluid models together with an extensive list of references on the relevant physics can be found in Ref. [29]).

At the wall, the density is left free, and the plasma-wall interaction is usually described in this model by the Bohm boundary conditions imposing an outgoing sonic/supersonic isothermal parallel velocity [3], i.e. $u \geqslant \sqrt{2k_B(T_{bc})/m_i}/(\rho_L\omega_0)$ or $u \leqslant -\sqrt{2k_B(T_{bc})/m_i}/(\rho_L\omega_0)$. On the dimensionless parallel momentum Γ, the condition becomes:

$$\begin{aligned} \Gamma &\geq +\sqrt{\frac{2T_{bc}}{T_0}}n \quad \text{if } \boldsymbol{b}\cdot\boldsymbol{n} > 0, \\ \Gamma &\leq -\sqrt{\frac{2T_{bc}}{T_0}}n \quad \text{if } \boldsymbol{b}\cdot\boldsymbol{n} < 0, \end{aligned} \tag{4}$$

where $\boldsymbol{n}$ is the outer normal to the wall surface. However, when magnetic field lines are almost tangent to the wall ($|\boldsymbol{b}\cdot\boldsymbol{n}| \approx 0$), the Bohm theory fails

ACCEPTED MANUSCRIPT

[29]. Hence, a threshold value t_h is defined in the present simulations, above which both the density and the momentum are left free, and a homogeneous Neumann condition $\partial_\perp(.) = 0$ is imposed. This threshold corresponds to $|\boldsymbol{b} \cdot \boldsymbol{n}| < 0.1$, i.e. to an angle in the poloidal plane between the magnetic field lines and the wall smaller than 5°. Note that the incidence angle used as threshold in a 3D geometry is much smaller (less than 0.1° in present simulations), the ratio ($\|\mathbf{B}_p\|/\|\mathbf{B}\|$) being much smaller than 1 in a tokamak.

When the computational domain is restricted to the plasma edge (Figures 1 a, b), boundary conditions are also required to model the interaction with the core. Dimensionless boundary conditions can be both of Dirichlet type, with $n = 1$ and $\Gamma = 0$, or of Neumann type with $\partial_\perp(.) = 0$.

3. Hybrid discontinuous Galerkin formulation

The magnetic topology in tokamak is complex and makes the flow strongly anisotropic. Eqs. 3 show that the flow in the parallel direction corresponds to a compressible adiabatic gas flow, whereas in the perpendicular direction it corresponds to an incompressible flow, dominated by turbulence process. Therefore, a specific HDG algorithm has been developed in this work.

Let's consider a computational domain Ω with physical boundary $\partial\Omega$ and a final time $T_f > 0$. Introducing the vector of conservative variable $\boldsymbol{U} = (n, nu)^{\mathrm{T}} = (U_1, U_2)^{\mathrm{T}}$ (the superscript T stands for the transpose), and the new unknown $\boldsymbol{\mathcal{G}} = \boldsymbol{\nabla U}$, Eqs. (3) can be recast into a system of first order equations

$$\begin{cases} \boldsymbol{\mathcal{G}} - \boldsymbol{\nabla U} = \mathbf{0} & \text{in } \Omega\times]0, T_f[, \\ \partial_t \boldsymbol{U} + \boldsymbol{\nabla}\cdot(\boldsymbol{\mathcal{F}} - D_f\boldsymbol{\mathcal{G}}) + \boldsymbol{\nabla}\cdot(D_f\boldsymbol{b}\otimes(\boldsymbol{b}\cdot\boldsymbol{\mathcal{G}}))+ & \\ \qquad \boldsymbol{\nabla}\cdot(\boldsymbol{U}\otimes\boldsymbol{u}_\perp) + \boldsymbol{g} = \boldsymbol{f} & \text{in } \Omega\times]0, T_f[, \\ \boldsymbol{U}(\boldsymbol{x}, 0) = \boldsymbol{U}_0 & \text{in } \Omega, \end{cases} \tag{5}$$

where $\boldsymbol{g} = (0, -c_s^2 U_1 \boldsymbol{\nabla}\cdot\boldsymbol{b})^{\mathrm{T}}$, $\boldsymbol{f} = (S_n, S_\Gamma)^{\mathrm{T}}$, and a set of appropriate initial conditions $\boldsymbol{U}_0$ is also considered. The diffusion tensor D_f is defined as

$$D_f = \begin{bmatrix} D & 0 \\ 0 & \mu \end{bmatrix},$$

ACCEPTED MANUSCRIPT

while the flux tensor $\boldsymbol{\mathcal{F}}(\boldsymbol{U})$ is

$$\boldsymbol{\mathcal{F}} = \begin{bmatrix} U_2 \boldsymbol{b}^{\mathrm{T}} \\ (\frac{U_2^2}{U_1} + c_s^2 U_1)\boldsymbol{b}^{\mathrm{T}} \end{bmatrix}.$$

The proper set of boundary conditions, corresponding to the plasma core and the plasma-wall interaction defined above, must also be supplied to system (5). They will be treated later.

The domain Ω is partitioned in $\mathtt{n_{el}}$ disjoint elements Ω_i with boundaries $\partial\Omega_i$, such that

$$\overline{\Omega} = \bigcup_{i=1}^{\mathtt{n_{el}}} \overline{\Omega}_i, \quad \Omega_i \cap \Omega_j = \emptyset \text{ for } i \neq j,$$

and the union of all $\mathtt{n_{fc}}$ faces (sides for 2D) is denoted as

$$\Sigma = \bigcup_{i=1}^{\mathtt{n_{el}}} \partial\Omega_i.$$

The discontinuous setting induces a new problem equivalent to (5), written as a system of first order partial differential equations, with some element-by-element equations and some global ones, namely, for $i = 1, \ldots, \mathtt{n_{el}}$

$$\left.\begin{aligned} \boldsymbol{\mathcal{G}} - \boldsymbol{\nabla} \boldsymbol{U} &= \boldsymbol{0} \\ \partial_t \boldsymbol{U} + \boldsymbol{\nabla}\cdot(\boldsymbol{\mathcal{F}} - D_f \boldsymbol{\mathcal{G}}) + \boldsymbol{\nabla}\cdot(D_f \boldsymbol{b} \otimes (\boldsymbol{b}\cdot\boldsymbol{\mathcal{G}})) + & \\ \boldsymbol{\nabla}\cdot(\boldsymbol{U} \otimes \boldsymbol{u}_\perp) + \boldsymbol{g} &= \boldsymbol{f} \end{aligned}\right\} \quad \text{in } \Omega_i \times]0, T_f[, \tag{6a}$$

$$\boldsymbol{U}(\boldsymbol{x}, 0) = \boldsymbol{U}_0 \qquad \text{in } \Omega_i, \tag{6b}$$

and

$$[\![\boldsymbol{U} \otimes \boldsymbol{n}]\!] = \boldsymbol{0} \qquad \text{on } \Sigma \backslash \partial\Omega \times]0, T_f[, \tag{6c}$$

$$[\![(\boldsymbol{\mathcal{F}} - D_f \boldsymbol{\mathcal{G}}) \cdot \boldsymbol{n}]\!] = \boldsymbol{0} \qquad \text{on } \Sigma \backslash \partial\Omega \times]0, T_f[, \tag{6d}$$

where $\boldsymbol{n}$ is the outer normal to the element face. The *jump* $[\![\cdot]\!]$ operator is defined at each internal face of Σ, i.e. on $\Sigma \backslash \partial\Omega$, using values from the elements to the left and right of the face (say, Ω_i and Ω_j), namely

$$[\![\circledcirc]\!] = \circledcirc_i + \circledcirc_j,$$

ACCEPTED MANUSCRIPT

and always involving the normal vector $\boldsymbol{n}$, see Ref. [30] for details. Thus, equation (6c) imposes the continuity of the unknowns across interior faces, while equation (6d) imposes the continuity of the normal component of the flux.

A major feature of HDG is that unknowns are restricted to the skeleton of the mesh, that is the union of all faces Σ. Here, the unknown field on the mesh skeleton Σ, is denoted $\widehat{\boldsymbol{U}}(\boldsymbol{x},t)$. The introduction of this new variable $\widehat{\boldsymbol{U}}(\boldsymbol{x},t)$ is crucial to define two types of problems: a local problem for each element and a global one for all faces.

3.1. The HDG local problem

The local element-by-element problem corresponds to the plasma model (3) on each element, with imposed Dirichlet boundary conditions on the element boundary. These imposed boundary values correspond to the unknowns $\widehat{\boldsymbol{U}}(\boldsymbol{x},t)$ for $\boldsymbol{x}\in\Sigma$.

Now the local element-by-element problem can be solved to determine $\boldsymbol{\mathcal{G}}$ and $\boldsymbol{U}$ in terms of the imposed $\widehat{\boldsymbol{U}}(\boldsymbol{x},t)$ on the mesh skeleton Σ. Thus, for $i=1,\ldots,\mathtt{n_{el}}$ the local HDG problem is solved,

$$\left.\begin{aligned}\boldsymbol{\mathcal{G}}-\boldsymbol{\nabla}\boldsymbol{U}&=\boldsymbol{0}\\ \partial_t\boldsymbol{U}+\boldsymbol{\nabla}\cdot(\boldsymbol{\mathcal{F}}-D_f\boldsymbol{\mathcal{G}})+\boldsymbol{\nabla}\cdot(D_f\boldsymbol{b}\otimes(\boldsymbol{b}\cdot\boldsymbol{\mathcal{G}}))+&\\ \boldsymbol{\nabla}\cdot(\boldsymbol{U}\otimes\boldsymbol{u}_\perp)+\boldsymbol{g}&=\boldsymbol{f}\end{aligned}\right\}\qquad \text{in } \Omega_i\times]0,T_f[, \tag{7a}$$

$$\boldsymbol{U}=\widehat{\boldsymbol{U}}\qquad \text{on } \partial\Omega_i\times]0,T_f[, \tag{7b}$$

$$\boldsymbol{U}(\boldsymbol{x},0)=\boldsymbol{U}_0\quad \text{in } \Omega_i. \tag{7c}$$

Notice that given the values of the conservative variables on Σ, $\widehat{\boldsymbol{U}}(\cdot,t)\in[\mathcal{L}^2(\Sigma)]^2$ for any instant $t\in[0,T]$, the same Dirichlet boundary condition is imposed to the left and right element of a given face. Consequently, the continuity of the unknowns (eq. (6c)) is ensured by eq. (7b).

The approximated solution is obtained after the corresponding discretization, see [18]. Two types of finite dimensional spaces must be defined, one for functions in the elements interior and another for trace functions, namely

ACCEPTED MANUSCRIPT

$$
\begin{aligned}
\mathcal{V}_t^h &:= \big\{ v : v(\cdot,t) \in \mathcal{V}^h \text{ for any } t \in [0,T_f] \big\}, \text{ with} \\
\mathcal{V}^h &:= \big\{ v \in \mathcal{L}^2(\Omega) : v|_{\Omega_i} \in \mathcal{P}^p(\Omega_i) \text{ for } i = 1, \ldots, \mathtt{n_{el}} \big\}, \text{ and} \\
\Lambda_t^h &:= \big\{ \hat{v} : \hat{v}(\cdot,t) \in \Lambda^h \text{ for any } t \in [0,T_f] \big\}, \text{ with} \\
\Lambda^h &:= \big\{ \hat{v} \in \mathcal{L}^2(\Sigma) : \hat{v}|_{\Gamma_i} \in \mathcal{P}^p(\Gamma_i) \text{ for } i = 1, \ldots, \mathtt{n_{fc}} \big\},
\end{aligned}
$$

where Γ_i is one face of the element and $\mathcal{P}^p$ denotes the space of polynomials of degree less or equal to p, see Remark 2 for details on the polynomial interpolation. To simplify the presentation, in an abuse of notation, the same notation is used for the numerical approximation, belonging to the finite dimensional spaces, and the exact solution, that is $\boldsymbol{U}$.

In order to derive a weak problem for system (7), the first two equations are respectively multiplied by a tensor test function $\boldsymbol{\mathcal{W}} \in [\mathcal{V}^h]^{2\times 2}$ and a vector test function $\boldsymbol{w} \in \mathcal{V}^h$, and the resulting equations are integrated in each element. After integrating by parts, the resulting weak problem for each element corresponding to (7) becomes: given $\widehat{\boldsymbol{U}} \in [\Lambda_t^h]^d$, find an approximation $(\boldsymbol{\mathcal{G}}, \boldsymbol{U}) \in [\mathcal{V}_t^h]^{d\times d} \times [\mathcal{V}_t^h]^d$ such that

$$
\begin{aligned}
\Big(\boldsymbol{\mathcal{W}}, \boldsymbol{\mathcal{G}}\Big)_{\Omega_i} - \Big(\boldsymbol{\nabla}\cdot\boldsymbol{\mathcal{W}}, \boldsymbol{U}\Big)_{\Omega_i} + \Big\langle \boldsymbol{\mathcal{W}}\cdot\boldsymbol{n}, \widehat{\boldsymbol{U}}\Big\rangle_{\partial\Omega_i} = 0 \\
\Big(\boldsymbol{w}, \partial_t \boldsymbol{U}\Big)_{\Omega_i} - \Big(\boldsymbol{\nabla}\boldsymbol{w}, \boldsymbol{\mathcal{F}} - D_f\boldsymbol{\mathcal{G}}\Big)_{\Omega_i} + \\
\Big\langle \boldsymbol{w}, \boldsymbol{\mathcal{F}} - D_f\boldsymbol{\mathcal{G}}\cdot\boldsymbol{n}\Big\rangle_{\partial\Omega_i} + \Big\langle \boldsymbol{w}, \tau(\boldsymbol{U} - \widehat{\boldsymbol{U}})\Big\rangle_{\partial\Omega_i} - \\
\Big(\boldsymbol{w}, D_f\boldsymbol{b}\otimes(\boldsymbol{b}\cdot\boldsymbol{\mathcal{G}})\Big)_{\Omega_i} + \Big\langle \boldsymbol{w}\cdot\boldsymbol{n}, D_f\boldsymbol{b}\otimes(\boldsymbol{b}\cdot\boldsymbol{\mathcal{G}})\Big\rangle_{\partial\Omega_i} - \\
\Big(\boldsymbol{w}, \boldsymbol{U}\otimes\boldsymbol{u}_\perp\Big)_{\Omega_i} + \Big\langle \boldsymbol{w}, (\boldsymbol{U}\otimes\boldsymbol{u}_\perp)\boldsymbol{n}\Big\rangle_{\partial\Omega_i} + \Big(\boldsymbol{w}, \boldsymbol{g}\Big)_{\Omega_i} = \Big(\boldsymbol{w}, \boldsymbol{f}\Big)_{\Omega_i},
\end{aligned}
\tag{8}
$$

for all $(\boldsymbol{\mathcal{W}}, \boldsymbol{w}) \in [\mathcal{V}_t^h]^{2\times 2} \times [\mathcal{V}_t^h]^2$, for $i = 1, \ldots, \mathtt{n_{el}}$, and with the initial condition defined in (7c). In (8) $\Big(\cdot,\cdot\Big)_{\Omega_i}$ denotes the $\mathcal{L}^2$ scalar product in the element Ω_i, $\Big\langle \cdot,\cdot \Big\rangle_B$ denotes the $\mathcal{L}^2$ scalar product of the traces over any $B \subset \Gamma$. The traces of $\boldsymbol{\mathcal{F}}$ and $\boldsymbol{\mathcal{G}}$ on the element boundaries have been replaced by the numerical traces in the following way

$$
\begin{aligned}
\widehat{\boldsymbol{\mathcal{F}}}\cdot\boldsymbol{n} &:= \boldsymbol{\mathcal{F}}\cdot\boldsymbol{n} + \tau(\widehat{\boldsymbol{U}} - \boldsymbol{U}), \\
\widehat{\boldsymbol{\mathcal{G}}} &:= \boldsymbol{\mathcal{G}},
\end{aligned}
\tag{9}
$$

ACCEPTED MANUSCRIPT

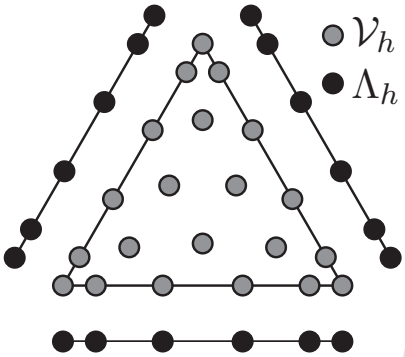

Figure 2: Example of nodal layout representing the spaces $\mathcal{V}^h$ and Λ^h for $p = 5$.

where τ is a stability parameter, see Remark 3 for a more detailed discussion.

Remark 2 (Polynomial interpolation). *Standard nodal basis are considered here, and Fekete node distributions are used to minimize ill-conditioning, see [31]. As an illustrative example, Figure 2 shows the nodes corresponding to the spaces $\mathcal{V}^h$ and Λ^h for a triangle with polynomial degree $p = 5$. However, other kind of interpolations could be considered.*

3.2. The HDG global problem

The local problems (7), or (8), allow to compute the solution $\boldsymbol{U}$ and $\boldsymbol{\mathcal{G}}$ in the whole domain in terms of the trace of the unknowns on the mesh skeleton, $\widehat{\boldsymbol{U}}$. Thus, this variable can now be understood as the actual unknown of the problem. This new unknown is determined using the global equation (6d). In fact, as already discussed, Eqs. (6c) is already fulfilled by the unicity of the trace unknown in each face (7b), and (6d) is the remaining global condition which must be imposed. This equation (in weak form) determine the HDG *global problem*. Namely, find an approximation $\widehat{\boldsymbol{U}} \in [\Lambda_t^h]^2$ such that

$$\sum_{i=1}^{\mathtt{n_{el}}} \left\langle \widehat{\boldsymbol{w}}, (\boldsymbol{\mathcal{F}} - D_f \boldsymbol{\mathcal{G}}) \cdot \boldsymbol{n} + \tau(\widehat{\boldsymbol{U}} - \boldsymbol{U}) \right\rangle_{\partial\Omega_i} + \left\langle \widehat{\boldsymbol{w}}, \boldsymbol{B} \right\rangle_{\partial\Omega} = \left\langle \widehat{\boldsymbol{w}}, \boldsymbol{t} \right\rangle_{\partial\Omega_N}, \quad (10)$$

for all $\widehat{\boldsymbol{w}} \in [\Lambda^h]^2$. Here, $\boldsymbol{U} \in [\mathcal{V}_t^h]^2$ and $\boldsymbol{\mathcal{G}} \in [\mathcal{V}_t^h]^{2\times 2}$ are now solutions of the local problems (8) as a function of $\widehat{\boldsymbol{U}}$, hence the only unknown in this equation is $\widehat{\boldsymbol{U}}$.

ACCEPTED MANUSCRIPT

In (10) $\boldsymbol{B}(\widehat{\boldsymbol{U}}, \boldsymbol{U}, \boldsymbol{\mathcal{G}})$ is a flux vector defined over the boundary $\partial\Omega$. Its precise definition depends on the type of boundary condition and will be given below.

Note that equation (6d) imposes continuity of the of the normal component of the flux on each element face, which induces (10) after using (9). Thus equation (10) weakly imposes the continuity of the normal flux.

Remark 3 (Stabilization tensor). *The stabilization parameter was introduced in* (9)*. Its influence is crucial and has been discussed and analyzed for a large number of problems by Cockburn and co-workers see, for instance, Refs. [13, 14, 15, 17, 16, 18]. Choosing the correct stabilization parameter should provide sufficient stabilization to the solution.*

3.3. Discrete boundary conditions

In tokamak edge simulations, boundary conditions describe, on one hand, the interactions of the edge plasma with the walls of the tokamak, and on the other hand, the flux of matter and momentum from the plasma core to the plasma edge.

3.3.1. Boundary condition at the core

For the boundary conditions at the core, two situations are considered, corresponding to the cases in which a volumetric source of mass and/or momentum is used or not.

If no volumetric source is considered, at the core the values of the density and the parallel momentum are imposed to reference values in a weak form. Hence, the numerical flux $\boldsymbol{B}$ is defined as

$$\boldsymbol{B} = \begin{Bmatrix} U_1^{ref} - \hat{U}_1 \\ U_2^{ref} - \hat{U}_2 \end{Bmatrix}.$$

In the numerical tests, these reference values are taken as $U_1^{ref} = 1$ and $U_2^{ref} = 0$.

If a volumetric source is applied, the boundary condition used at the core is of homogeneous Neumann type, that is, the gradient of the conservative variables is set to zero in the direction normal to the boundary. This condition translates to setting the numerical flux $\boldsymbol{B}$ in the following way

$$\boldsymbol{B} = \boldsymbol{\mathcal{G}} \cdot \boldsymbol{n},$$

which turns out in setting the quantity $\boldsymbol{\mathcal{G}} \cdot \boldsymbol{n}$ to zero weakly on the boundary faces.

ACCEPTED MANUSCRIPT

3.3.2. Wall boundary conditions

The plasma wall interaction is usually described by the Bohm boundary conditions eq. (4), which require an outgoing sonic/supersonic isothermal velocity at the wall.

Since the Bohm boundary condition is not affecting the value of the density at the boundary, the first component of the vector $\boldsymbol{B}$ can be set as

$$B_1 = (U_1 - \hat{U}_1) - \{\boldsymbol{\mathcal{G}} \cdot \boldsymbol{n}\}_1,$$

which imposes weakly the value of the trace solution of the density $\hat{U}_1$ to the nodal value computed in the domain U_1, and a zero derivative normal to the boundary.

The second component of $\boldsymbol{B}$ must impose the inequality defined in eq. (4). This means that the parallel momentum must be imposed to the value $s_n U_1$, where $s_n = \text{sign}(\boldsymbol{b} \cdot \boldsymbol{n})$, only if the parallel velocity u is subsonic. If the estimated parallel velocity is sonic/supersonic, no boundary condition is imposed and the outgoing velocity is free. In such way, the hyperbolic problem is mathematically well-posed as precised in Ref. [32].

This is achieved using a switch parameter δ, which determines if the trace unknown relative to the parallel momentum is set to the value computed in the domain or to the sonic value,

$$B_2 = (1-\delta)(U_2 - \hat{U}_2) + \delta(s_n U_1 - \hat{U}_2) - (1-\delta)\{\boldsymbol{\mathcal{G}} \cdot \boldsymbol{n}\}_2,$$

The δ parameter is set to 0 if $s_n u \geq 1$ and to 1 if $s_n u < 1$, see Fig3. Notice that, when the trace parallel momentum variable is taken equal to the value computed in the domain (hence for $\delta = 0$), the normal gradient of $\hat{U}_2$ is also set to zero.

However, the hypothesis of the Bohm theory leading to eq. (4) fail when the magnetic field is almost tangent to the wall. Hence, a threshold t_h is defined, below which the eq. (4) must not be applied. This is achieved modifying the setting of the switch δ in the following way

$$\delta = 0 \text{ if } |\boldsymbol{b} \cdot \boldsymbol{n}| < t_h \text{ or } s_n u \geq 1,$$
$$\delta = 1 \text{ if } |\boldsymbol{b} \cdot \boldsymbol{n}| \geq t_h \text{ and } s_n u < 1.$$

3.4. Shock-capturing

The system of equation (3) being hyperbolic in the magnetic field direction, strong gradients of the parallel velocity may appear in the solutions,

ACCEPTED MANUSCRIPT

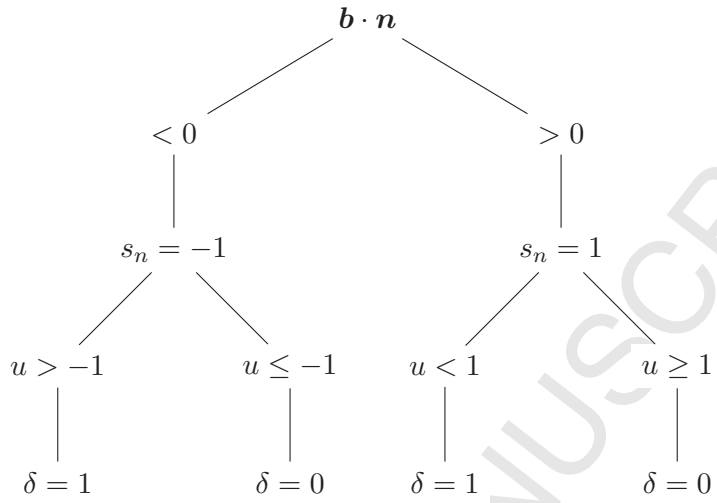

Figure 3: Decision tree to set switch parameter δ in the Bohm boundary condition.

possibly associated to shocks. Dealing with such solutions is a challenging task with high-order methods because they are known to produce spurious Gibbs-type oscillations. Several approaches exist in the literature to capture shocks with high-order approximations, most of them being based on slope limiters, possibly of high-order [33], on filtering to the solution [34], on the selective application of viscosity to the different spectral scales [35], or on reconstructing technique from the unlimited oscillatory solution [36]. Differently in Ref. [37], the authors proposed an approach which sizes the local entropy production to add nonlinear viscosity in the computation.

In the present work, the shock-capturing technique is inspired by Ref. [38], and it is based on the introduction of an isotropic diffusion term in the system. The second equation of the local problem (7) is therefore modified accordingly as

$$\partial_t \boldsymbol{U} + \boldsymbol{\nabla}\cdot(\boldsymbol{\mathcal{F}} - D_f\boldsymbol{\mathcal{G}}) + \boldsymbol{\nabla}\cdot(D_f\boldsymbol{b}\otimes(\boldsymbol{b}\cdot\boldsymbol{\mathcal{G}})) + \boldsymbol{\nabla}\cdot(\boldsymbol{U}\otimes\boldsymbol{u}_\perp) + \boldsymbol{g} = \boldsymbol{f} + \boldsymbol{\nabla}\cdot(\varepsilon\boldsymbol{\nabla}\boldsymbol{U}) \tag{11}$$

where the parameter ε controls the amount of artificial diffusion.

Here, the computation of ε is driven by a discontinuity sensor which is

ACCEPTED MANUSCRIPT

evaluated element by element using the parallel velocity field as

$$S_i = \frac{\Big(u - \tilde{u}, u - \tilde{u}\Big)_{\Omega_i}}{\Big(u, u\Big)_{\Omega_i}},$$

where $\tilde{u}$ is a modified parallel velocity obtained truncating the modal expansion of the elemental solution to the terms up to order $p-1$.

Once computed the discontinuity sensor, an element-wise artificial diffusion is computed as $\varepsilon_i = \varepsilon_i(S_i)$ as

$$\varepsilon_i = \begin{cases} 0 & \text{if} \quad s_i < s_0 - \kappa, \\ \dfrac{\varepsilon_0}{2}\Big(1 + \sin\dfrac{\pi(s_i - s_0)}{2\kappa}\Big) & \text{if} \quad s_0 - \kappa < s_i < s_0 + \kappa, \\ \varepsilon_0 & \text{if} \quad s_i > s_0 + \kappa, \end{cases}$$

where $s_i = \log_{10}(S_i)$, $s_0 = \log_{10}(1/p^4)$ while κ and $\varepsilon_0 \sim h/p$ are chosen empirically to obtain a sharp shock profile while avoiding oscillations, see Ref. [38] for more details.

The element-wise values are then used to compute a continuous field $\varepsilon(\boldsymbol{x})$ by computing for each vertex the maximum ε_i for all the neighboring elements, and then linearly interpolating in each element interior.

3.5. Discrete form of the weak equations

The evaluation of the integrals in (8) and (10) by means of Gaussian quadrature leads to the semi-discrete form of the HDG scheme.

Remark 4 (Gauss quadrature). *Numerical integration on triangle is obtained using the optimized symmetric quadrature rules described in [39]. For curved elements,a quadrature of higher-order than required on straight boundaries is chosen in order to avoid integration errors produced by non-constant Jacobians. This point is confirmed by the verification tests (Section 4), which have been performed on curved elements.*

For the local problem, the system

$$\boldsymbol{M}_i \frac{d\boldsymbol{U}}{dt} + \boldsymbol{R}_i(\boldsymbol{U}, \boldsymbol{\mathcal{G}}, \widehat{\boldsymbol{U}}) = \boldsymbol{f}_i, \quad \text{for } i = 1, \ldots, \mathtt{n_{el}} \tag{12}$$

ACCEPTED MANUSCRIPT

is obtained, where $\boldsymbol{M}_i$, $\boldsymbol{R}_i(\boldsymbol{U},\boldsymbol{\mathcal{G}},\widehat{\boldsymbol{U}})$ and $\boldsymbol{f}_i$ are respectively the mass matrix, the residual and the discrete right-hand-side of the i_{th} element. System (12) can be efficiently discretized in time with an implicit time integrator, such as backward Euler, a Backward Differentiation Formula, or a diagonally implicit Runge-Kutta method, see [18], producing the non-linear algebraic system

$$\alpha\frac{\boldsymbol{M}_i}{\Delta t}\boldsymbol{U}^n + \boldsymbol{R}_i(\boldsymbol{U}^n,\boldsymbol{\mathcal{G}}^n,\widehat{\boldsymbol{U}}^n) = \boldsymbol{f}_i^n - \boldsymbol{M}_i W(\boldsymbol{U}^{n-1},\boldsymbol{U}^{n-2},\ldots,\boldsymbol{U}^{n-j},\Delta t), \quad \text{for } i=1,\ldots,\mathtt{n_{el}}$$

where α, j and W are respectively a constant, the number of steps and a function specific of the time integration scheme. The non-linear residual $\boldsymbol{R}_i(\boldsymbol{U},\boldsymbol{\mathcal{G}},\widehat{\boldsymbol{U}})$ is linearized using the fact that system (5) are *homogeneous functions of degree 1* (see [40]), so the flux can be computed as

$$\boldsymbol{\mathcal{F}}(\boldsymbol{U}) = \frac{d\boldsymbol{\mathcal{F}}(\boldsymbol{U})}{d\boldsymbol{U}}\boldsymbol{U}, \tag{13}$$

where the Jacobian is a third order tensor with components

$$\mathbb{A}(\boldsymbol{U}) = \frac{d\boldsymbol{\mathcal{F}}(\boldsymbol{U})}{d\boldsymbol{U}} = \begin{bmatrix} \boldsymbol{0} & \boldsymbol{b} \\ (-\frac{U_2^2}{U_1^2} - c_s^2)\boldsymbol{b} & 2\frac{U_2}{U_1}\boldsymbol{b} \end{bmatrix}.$$

Relation (13) induces a Newton-Raphson (NR) iterative scheme for the computation of the residual, with the form

$$\boldsymbol{R}_i(\boldsymbol{U}^r,\boldsymbol{\mathcal{G}}^r,\widehat{\boldsymbol{U}}^r) = \boldsymbol{R}_i(\mathbb{A}(\boldsymbol{U}^{r-1})\boldsymbol{U}^r,\boldsymbol{\mathcal{G}}^r,\mathbb{A}(\widehat{\boldsymbol{U}}^{r-1})\widehat{\boldsymbol{U}}^r), \tag{14}$$

where r is the NR iteration. This procedure allows to solve for the variable $\boldsymbol{U}$ and $\boldsymbol{\mathcal{G}}$ in each element as a function of the variable $\widehat{\boldsymbol{U}}$ in the faces of the element, that is

$$\begin{aligned} \mathcal{U}_i^{n,r} &= \mathbf{U}_i^{r,n}\Lambda_i^{n,r} + \mathcal{F}_i^{r,n}, \\ \mathcal{G}_i^{n,r} &= \mathbf{G}_i^{r,n}\Lambda_i^{n,r} + \mathcal{H}_i^{r,n}, \quad \text{for } i=1,\ldots,\mathtt{n_{el}}, \end{aligned} \tag{15}$$

where $\mathcal{U}_i^{n,r}$, $\mathcal{G}_i^{n,r}$ and $\Lambda_i^{n,r}$ are respectively the nodal solutions of the unknown $\boldsymbol{U}$, $\boldsymbol{\mathcal{G}}$ for the element Ω_i and the nodal solution of the trace $\widehat{\boldsymbol{U}}$ for the faces of the element Ω_i, at the time step n and NR iteration r. The terms $\mathbf{U}_i$ and $\mathbf{G}_i$ are the elemental matrices while $\mathcal{F}_i$ and $\mathcal{H}_i$ are the right-hand-side vectors for the two systems.

ACCEPTED MANUSCRIPT

The global problem (10) is also linearized using (13), while the terms involving the variable $\boldsymbol{U}$ and $\boldsymbol{\mathcal{G}}$ are replaced using the solution of the local problem (15). Thus, a set of algebraic equations involving only the nodal values of the variable $\widehat{\boldsymbol{U}}$ in the whole mesh skeleton is obtained

$$\mathbf{K}^{r,n}\Lambda^{r,n} = \mathcal{R}^{r,n}, \tag{16}$$

where $\mathbf{K}^{r,n}$ is the global matrix and $\mathcal{R}^{r,n}$ is the global right-hand-side for each NR iteration and each time step.

Therefore, the solution procedure is the following:

- initialize the solution
- for each time step:
  - for each NR iteration and until convergence:
    - solve the local problem (15) for each element, obtaining $\mathcal{U}_i^{n,r}$ and $\mathcal{G}_i^{n,r}$ as a function of $\Lambda_i^{n,r}$;
    - solve the global problem (16), obtaining $\Lambda^{n,r}$;
    - compute the elemental solution $\mathcal{U}_i^{n,r}$ and $\mathcal{G}_i^{n,r}$ in each element;
    - check convergence;
  - update the solution and advance in time.

Steady solutions can be also computed by neglecting time derivative in eq. (8). This will be used to rapidly compute equilibria that will be used afterwards as initial conditions.

4. Code verification

The method of the manufactured solution is used to perform convergence tests on unstructured triangular meshes composed of curved elements like shown in Figure 4. Tests are performed on a 2D circular domain centered in $\boldsymbol{x} = (0.5, 0.5)$. All boundary conditions are Dirichlet boundary conditions. The analytical solution is the following:

$$\begin{aligned} n_a &= 2 + \sin(2\pi\omega_x x)\sin(2\pi\omega_y y), \\ u_a &= \cos(2\pi\omega_x x)\cos(2\pi\omega_y y), \end{aligned}$$

ACCEPTED MANUSCRIPT

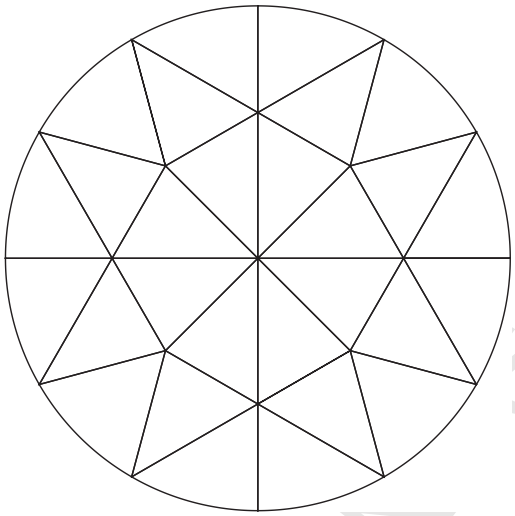

Figure 4: Example of mesh with curved elements in a circular geometry for $h = 1/4$ and $p = 4$.

with ω_x and ω_y the number of waves in the x and y directions. Corresponding source terms S_{n_a} and S_{Γ_a} are considered in Eq. (3). The non-divergence-free poloidal magnetic field is chosen as

$$b_x = \frac{1}{30}(x - y^2 + 2),$$
$$b_y = \frac{1}{30}(xy + y),$$

and a value of the dimensionless sound speed $c_s = 10$ is taken. The steady state version of the equations is used.

Convergence tests are performed both using h-refinement (mesh refinement) and p-refinement (polynomial degree increase).

In the h-refinement tests, the characteristic length of elements (h) is decreased dividing each element in two without changing the type of elements used, $h = 1/2^m$, for $m = 1, \ldots, 5$. Tests are carried out for various polynomial degrees $p = 1, \ldots, 5$. Results are depicted in Figures 5, and show the expected convergence slope $p + 1$ whatever the polynomial degrees.

In all p-refinement tests the mesh is the same, and the polynomial degree is increased. Results on Figure 6 show the expected exponential rate of convergence.

ACCEPTED MANUSCRIPT

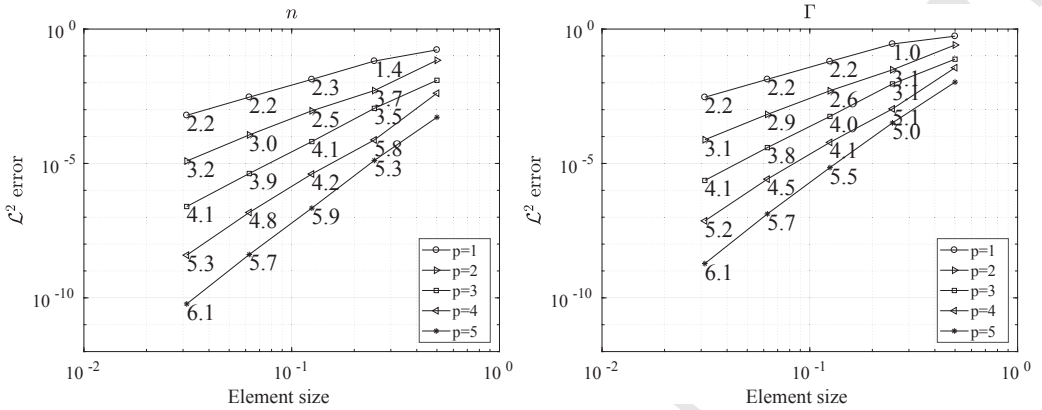

Figure 5: h-convergence tests showing the $p+1$ rate of convergence for the density (left) and parallel momentum (right). Evolution of the L^2-errors when refining meshes for 5 different polynomial degrees p. The values indicate the local slope between two successive points. Circular geometry with curved elements. $\omega_x = 1$ and $\omega_y = 1$, $D = \mu = 1$.

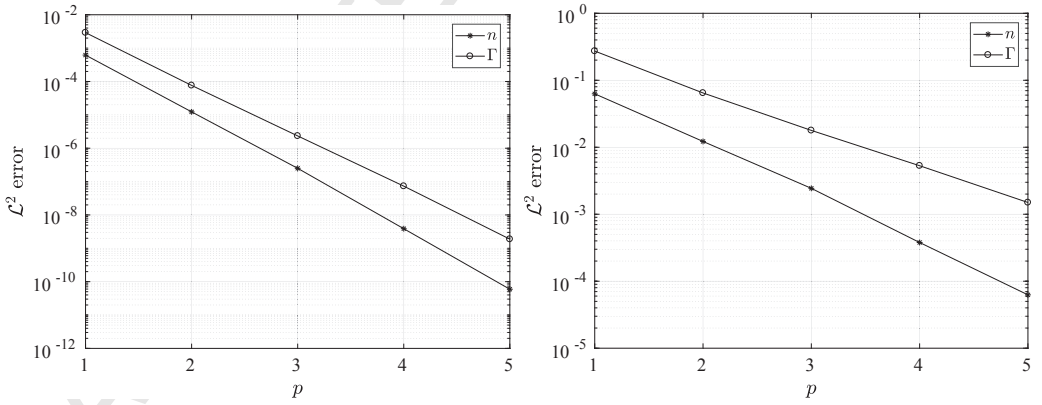

Figure 6: p-convergence tests showing the exponential rate of convergence for the density (left) and parallel momentum (right). Circular mesh (left) and WEST mesh (right). $\omega_x = 1$ and $\omega_y = 1$, $D = \mu = 1$.

ACCEPTED MANUSCRIPT

5. Code validation

The new HDG solver has been first benchmarked with SOLEDGE2D [1] in a realistic WEST (acronym derived from W Environment in Steady-state Tokamak) geometry [27]. WEST is an upgrade of the Tore Supra tokamak equipped with an actively cooled tungsten divertor using the same design as the ITER one. It is a medium size tokamak. Developed by the same authors, SOLEDGE2D is today a well-referenced transport code in the magnetic fusion international community.

Other computations have been performed thereafter in a circular geometry (Figure 1) to estimate the scrape-off layer width when varying the imbalance between diffusive and drift-based cross-field transport. Numerical results show the capability of the solver to deal with low diffusive solutions, and are coherent with theoretical predictions recently provided by the heurisitc model of Goldston [41].

5.1. Code benchmarking in WEST geometry

The geometry of WEST shown on Figure 1 is demanding for numerics. The magnetic geometry with two X-points is complex to deal with, particularly when using flux-surface aligned meshes as in most of the solvers of the literature. In addition, the shape of the first wall is elaborated with sharp edges and corners as well as small cavities around. The mesh is composed here of 30876 $p8$-elements, locally refined near the tokamak wall (Figure 1) in order to prevent negative values in this flow region where density can be very low. Let's notice that the mesh size has not been optimized in the computations. In this benchmarking exercise, the model is given by Eq.3 without drift ($\mathbf{u}_\perp \equiv 0$), the cross-field transport being so purely diffusive. The constant background temperature is $T_{bc} = 50eV$ and the magnetic field magnitude at the magnetic axis is $B_a = 3.6$Tesla.

The solution of reference is provided by SOLEDGE2D, which is based on an unsteady structured mesh solver (second-order finite-differences scheme) with flux-surface aligned coordinates. In the present test, the mesh is composed of 30000 points. A specific feature of SOLEDGE2D is the use of an original penalization technique [42] to model the tokamak wall instead of a set of classical mathematical boundary conditions.

The diffusion coefficients are gradually reduced to $D = \mu = 0.038$ ($= 1m^2s^{-1}$). The Newton-Raphson algorithm is initialized with the solution obtained at the previous diffusion value. For each diffusion value, the HDG

ACCEPTED MANUSCRIPT

steady solver converges fast in only few iterations. As a consequence, the equilibrium is reached in few tens of minutes on 36 CPU, to be compared to few hours using the unsteady solver of SOLEDGE2D.

Contour plots of density n and parallel Mach number $M_\parallel$, (that is, the ratio of the plasma parallel velocity along the field lines and the acoustic velocity) computed by the two codes, are shown on Figure 7 in the WEST poloidal cross-section. The HDG solution (on the right) shows a close agreement with the solution of reference computed with SOLEDGE2D (on the left). The large scales flows are well predicted by the HDG into the entire tokamak cross-section. The particles density is maximum at the core boundary, where the Dirichlet condition $n = 1$ is applied, and rapidly decreased to low values in the scrape-off layer (SOL) beyond the separatrix. The parallel Mach number distributions show also very similar trends with similar locations for positive and negative Mach number values and a flow reversal around midplane. As expected from theoretical analysis by Ghendrih *et al.* [43], and from numerical investigations by Bufferand *et al.* [44] , both solutions exhibit transitions to supersonic flows in the vicinity of both divertor legs, Figure 7. A zoom on the $M_\parallel$ distribution around the separatrix within the divertor area on Figure 8 shows that both codes predict the transition to supersonic flows at about the same location. A more quantitative comparison is also provided by plotting density and parallel Mach number profiles on Figure 9. The radial profiles of n at midplane show an excellent agreement between the two solutions, on both low and high magnetic field sides. The parallel profiles of $M_\parallel$ along the magnetic field line located in the vicinity of the separatrix in the SOL also show good agreement, with values larger than the sound speed in the close vicinity of the targets on both sides. The new HDG solution does not exhibit any numerical oscillations.

5.2. Scrape-off layer width estimate

To challenge the code with low physical diffusion solutions, we analyse how the HDG solver is able to predict the dependence of the scrape-off layer width, $\lambda_n = |\partial \ln n/\partial r|^{-1}$, with respect to the intensity of the drift-based convective transport. λ_n is determined by a competition between cross-field and parallel transport and sets the available volume for power dissipation and the deposition area of the exhaust power at the divertor targets. In high confinement mode (H-mode), the mechanism driven by the perpendicular transport in the vicinity of the separatrix is however not clear, the turbulence being strongly reduced in the pedestal. The scaling of λ_n, with the plasma

ACCEPTED MANUSCRIPT

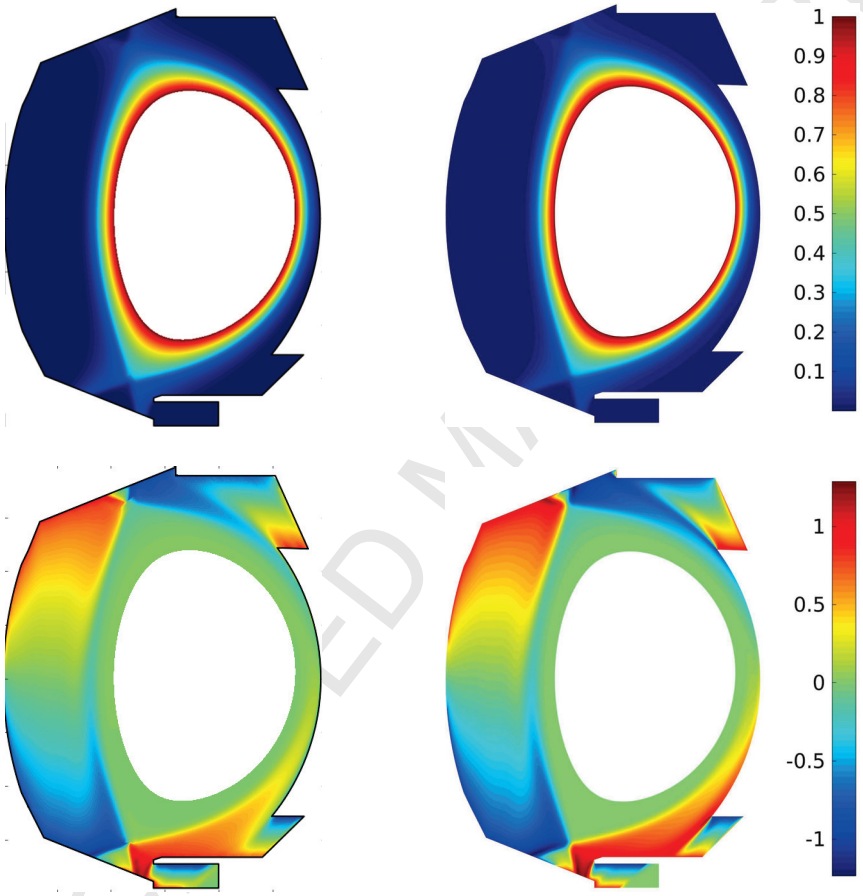

Figure 7: Solutions benchmarking in WEST. Large scale flows predicted by SOLEDGE2D (left) and the new HDG solver (right). Isolines of density n (top) and parallel Mach number $M_{\parallel}$ (bottom). Computations are carried out here with no curvature drift. $D = \mu = 0.038(= 1m^2s^{-1})$. Background temperature $T_{bc} = 50eV$ and $B_a = 3.6$Tesla at the magnetic axis.

ACCEPTED MANUSCRIPT

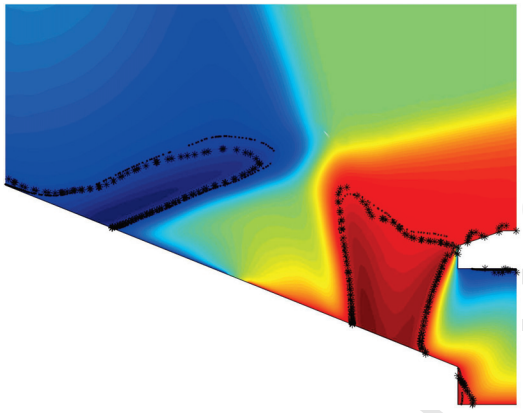

Figure 8: Solutions benchmarking in WEST. Zoom on the parallel Mach number $M_{\|}$ around the separatrix within the divertor area. The black lines show the transition to supersonic flows predicted by the two codes: SOLEDGE2D solution (*), HDG solution (black points). Computations are carried out with no curvature drift. $D = \mu = 0.038(= 1m^2s^{-1})$. Background temperature $T_{bc} = 50eV$ and $B_a = 3.6$Tesla at the magnetic axis.

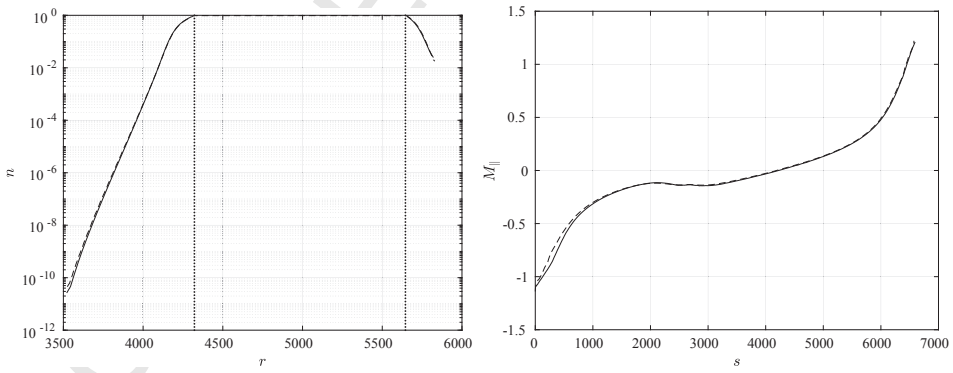

Figure 9: Solutions benchmarking in WEST. Radial density profiles at midplane (top), and parallel profiles of parallel Mach number $M_{\|}$ along a magnetic field line within the SOL and close to the separatrix (bottom). s defines the curvilinear coordinate along the magnetic field line. HDG solution (solid line) and SOLEDGE2D solution (dashed line). Computations are carried out with no curvature drift. $D = \mu = 0.038(= 1m^2s^{-1})$. Background temperature $T_{bc} = 50eV$ and $B_a = 3.6$Tesla at the magnetic axis.

ACCEPTED MANUSCRIPT

parameters is thus a key issue for the success of the fusion operation regarding on the heat extraction.

The intensity of the cross-field convective transport is modulated in the present model by varying the diffusion D ($D = \mu$). For low diffusion solutions, the parallel transport becomes dominant, which favor field-aligned meshes for the discretization. On the contrary, when the mesh is no longer aligned along the magnetic field lines, these solutions can be very demanding for the solver.

Computations have been performed in a circular geometry with an infinitively thin limiter located at the bottom of the poloidal section. Such a limiter shape avoids the use of ill-defined perpendicular boundary conditions on the roof, while providing similar SOL plasma parameters (like the density value at the separatrix or the radial decay length) to those of the finite size limiter configuration, as we have shown in former computations (see for example in Ref.[45]). On both sides of the thin limiter, the sheath boundary conditions defined above in Section 2 are applied. The large radius of the tokamak is here equal to $R_0 = 1.075m$, with a plasma radius $a = 0.287m$. The constant background temperature is $T_{bc} = 50eV$ and the magnetic field magnitude at the axis is $B_a = 1$Tesla. In such a circular geometry the magnetic field is analytical with poloidal and toroidal magnetic field magnitudes equal to

$$\|\mathbf{B}_p\| = \frac{B_a r}{Rq\sqrt{1-(\frac{r}{R_0})^2}},$$
$$\|\mathbf{B}_\phi\| = \frac{B_a R_0}{R}.$$

where r is the small radius of the tokamak (radius of the poloidal corss-section) and $R(r)$ defines the radial coordinate along the horizontal axis. In the following simulations, a constant security factor $q = 3.5$ is used.

The dimensionless diffusion coefficients D and μ vary between 10^{-1} ($= 2.6m^2s^{-1}$) and 10^{-4} ($= 2.6 \times 10^{-3}m^2s^{-1}$) (drift-dominated regime). Purely diffusive solutions have been also computed by cancelling the velocity drift in the model, that corresponds to $\mathbf{u}_\perp \equiv 0$. When decreasing diffusion coefficients, the mesh has had to be successively refined, particularly around the separatrix, from 10244 to 11760 $p = 10$ elements and the limiter height decreased to avoid too low density values in Eq. 3 (close to zero machine) in the far SOL. The steady solver (Newton-Raphson algorithm) has been used

ACCEPTED MANUSCRIPT

for all computations at large diffusion. In the drift-based dominated regimes ($D < 10^{-3}$), however, unsteadiness occurs that requires to use the temporal solver including the shock-capturing scheme presented in Section 3.4.

Contour plots and profiles of $M_{\parallel}$ at low diffusion ($D = 10^{-3}$) are shown both in a purely diffusive ($\boldsymbol{u}_{\perp} \equiv 0$) and a drift-dominated regime on Figure 10. Without drift-based transport (Figure 10a), and at low diffusion, the flow is purely driven in the parallel direction by the limiter which acts as a sink for the particles. The Bohm boundary condition on both sides of the limiter leads to a $M_{\parallel}$ larger or equal to 1. Both solutions are non symmetric with respect to the limiter, but with a stagnation point, corresponding to a zero Mach number, which remains located around the top of the tokamak cross-section. In the purely diffusive regime the asymmetry of the solution is only related to the curvature terms related to the magnetic geometry. When drift-based cross-field transport is considered, the flow is modified by the occurrence of a flow reversal due to Pfirsch-Schlüter parallel flows, which arise to compensate the non-divergence free poloidal drift flow, Figure 10b. When the drift-based cross-field transport becomes dominant (low diffusion) (Figure 10b), the Pfirsch-Schlüter parallel flows become responsible for the majority of the observed parallel flows in the outboard and inboard midplane vicinity. They lead to the occurence of locally supersonic flows, mainly located in the SOL and at the top of the machine. As theoretically explained in Ghendrih *et al.* [43], these supersonic flows are induced by particles and momentum sinks in the SOL, resulting from drift-based radial transport, and which are no longer compensated by the diffusive perpendicular transport. The same feature was recently observed in Reiser and Eich [46] in a X-point model geometry. The shock-capturing technique, introduced in Section 3.4, acts at the locations of the front corresponding to the transition to supersonic flow, as shown by the contour plots of the ε parameter on Figure 11. Indeed, non-zero ε values match very well with the front shape emphasized by the $M_{\parallel}$ contours on Figure 10 b.

The log-log plot of the averaged value of the numerically obtained decay length is shown for the two models with or without ($\boldsymbol{u}_{\perp} \equiv 0$) drift, and for different values of the diffusion ranging from 10^{-1} to 10^{-4}, Figure 10. In the diffusive radial transport regime, λ_n decays linearly with D in the log-log plot, with a slope equal to 1/2 in agreement with theory ($\lambda_n \sim D^{1/2}$). When the transport becomes dominated by drifts, that corresponds in our simulation parameters to $D < 10^{-3}$, the decay of λ_n with D is much slower, with a slope equal to about 0.1. The transition to this new regime corresponds to a

ACCEPTED MANUSCRIPT

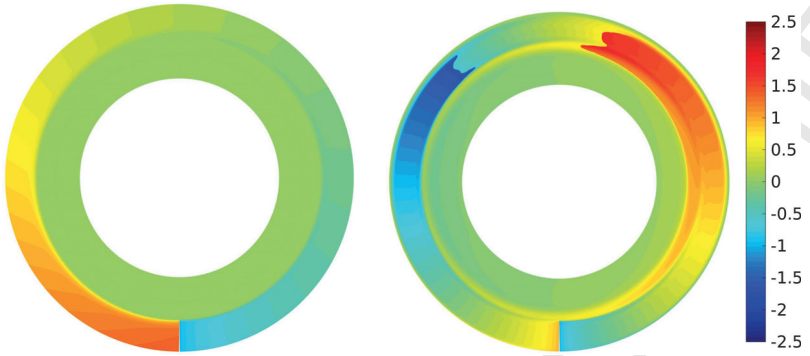

Figure 10: Parallel Mach number $M_{\|}$ contours in circular tokamak cross-section: purely diffusive ($\boldsymbol{u}_{\perp} \equiv 0$) (a) and drift-dominated (b) radial transport regime. $D = \mu = 10^{-3} (= 2.6 \times 10^{-2} m^2 s^{-1})$. Background temperature $T_{bc} = 50eV$ and magnetic field magnitude at the axis $B_a = 1$Tesla.

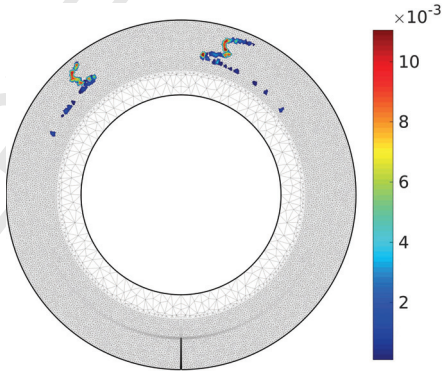

Figure 11: Contours plot in the poloidal plane of the ϵ coefficient of Eq. 11 used in the shock-capturing technique. Non zero values of ϵ match very well the front corresponding to the supersonic flow transition on Figure 10 . $D = \mu = 10^{-3} (= 2.6 \times 10^{-2} m^2 s^{-1})$. Backfround temperature $T_{bc} = 50eV$ and magnetic field magnitude at the axis $B_a = 1$Tesla.

ACCEPTED MANUSCRIPT

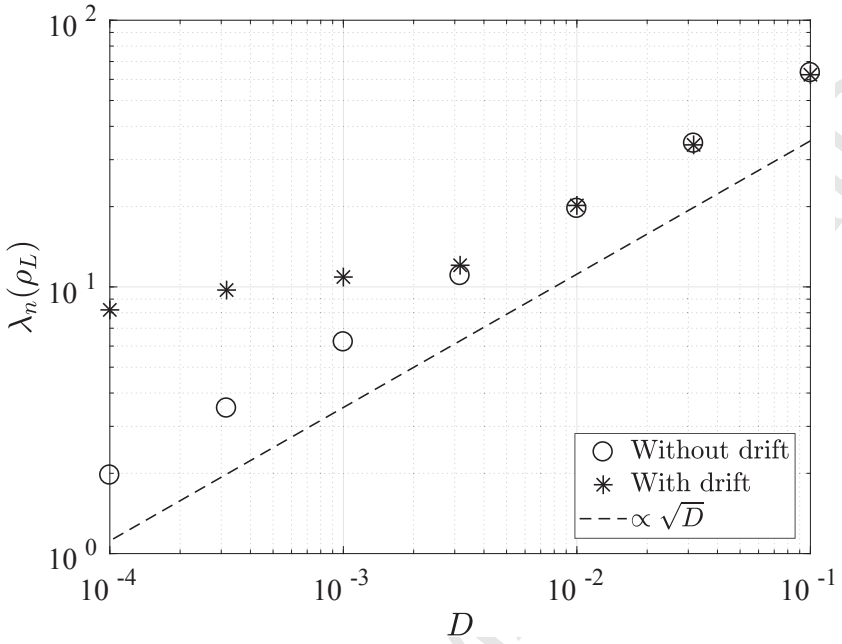

Figure 12: Log-log plot of the dimensionless decay length λ_n as a function of the diffusion coefficient. The two models with and without drift-based radial flow are considered. Circular geometry. Background temperature $T_{bc} = 50eV$ and magnetic field magnitude at the axis $B_a = 1$Tesla. The dimensionless diffusion coefficients D ($D = \mu$) varies between 10^{-1} ($= 2.6m^2s^{-1}$) and 10^{-4} ($= 2.6 \times 10^{-3}m^2s^{-1}$) (drift-dominated regime).

strong increase of the Pfirsch-Schlüter parallel flows intensity, with supersonic parallel velocities close to the top of the machine, as shown on Figure 13.

This result is coherent with the heuristic model recently proposed by Goldston [41], and which suggests that the width of the scrape-off layer might depend on how rapidly plasma moves across the magnetic field – due to well-understood classical "drifts".

This analysis shows the capacity of the new solver to accurately simulate low diffusion solutions with high supersonic velocities.

6. WEST simulations extended to the plasma center: effects on the transport

In the hot core plasma kinetic effects are dominant, and fluid codes usually exclude the tokamak core region. However, the arbitrary inner boundary conditions presently used in the edge simulations are not fully satisfactory.

ACCEPTED MANUSCRIPT

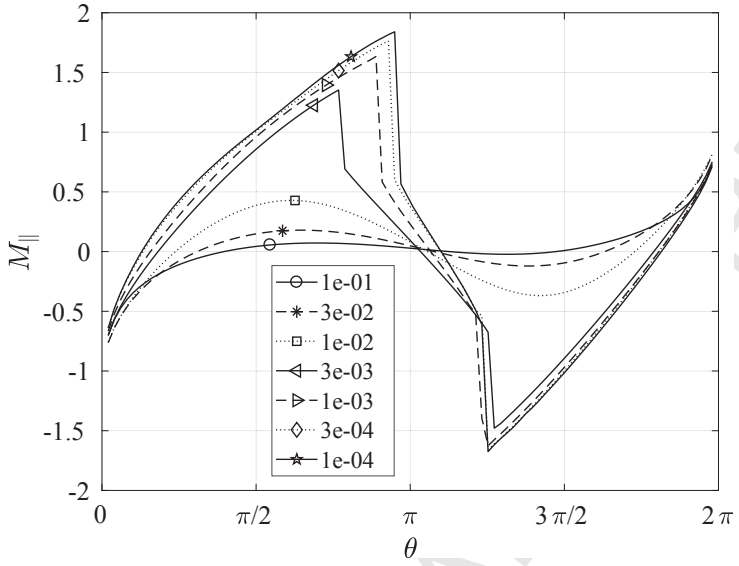

Figure 13: Parallel profiles of the parallel Mach number $M_{\|}$ close to the separatrix into the SOL at $r = 0.3$, when decreasing the diffusion from 10^{-1} to 10^{-4} (from $2.6m^2s^{-1}$ to $2.6 \times 10^{-3}m^2s^{-1}$). θ is the poloïdal angle. $\theta = 0$ (2π) corresponds to the limiter location. Circular geometry. Background temperature $T_{bc} = 50eV$ and magnetic field magnitude at the axis $B_a = 1$Tesla.

Extending simulations up to the center can be relevant in order to reduce the number of free parameters by replacing inner boundary conditions by fluxes imposed by the physics of the heating systems. Furthermore, such new simulations would provide a key asset to assess compatibility between exhaust and core confinement for a given scenario. With the numerical methods usually implemented in the edge code solvers, and based on field-aligned structured meshes, the code extension is not straightforward. The numerical issues are related to the singularity of the magnetic geometry at the center, and the constraint on the CFL condition due to the shrinkage of the grid cells. On the contrary, the present HDG solver can be straightforwardly extended to the center. Preliminary simulations in the WEST geometry give us a flavor of the interest of such simulations.

Simulations have been performed in both configurations, with inner hole and without, Figure 14. Background temperature and magnetic field magnitude at the axis are equal to $T_{bc} = 200eV$ and $B_a = 3.6$Tesla, respectively. Simulations in the whole cross-section of the tokamak require to add a volumetric source of particles in order to balance the particles lost at the wall,

ACCEPTED MANUSCRIPT

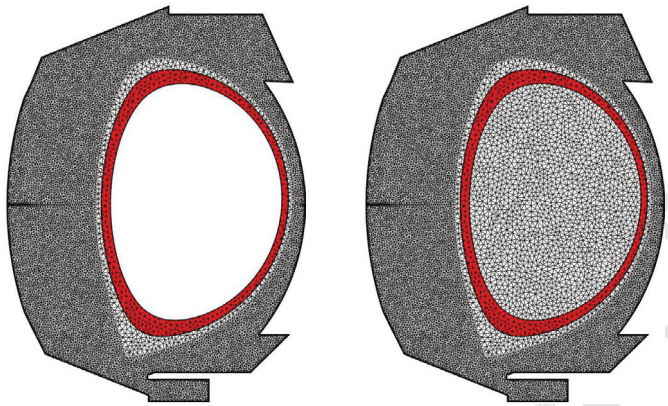

(a) (b)

Figure 14: West configuration for two meshes: with inner hole (a) and without (b). The red areas show the particles source locations. The integral of the source is equal to 1 (non-dimensional units).

and to reach a steady state. The same source has been added in the simulations with the hole, as shown on Figure 14. In this case, homogeneous Neumann boundary conditions for n and Γ are used at the inner boundary of the domain.

To deal with negative density values that could appear at some nodes in such simulations, a threshold value is used at each iteration of the Newton-Raphson algorithm. In addition, since oscillations between nodes may also lead to negative values of the density values at the Gauss point a second check is done during the calculation of the Jacobian (14).

For this range of control parameters, the two solutions are qualitatively similar in the common plasma region, as shown by the contour plots of the density and the parallel Mach number $M_{\|}$ on Figure 15. More quantitatively, the relative differences in density and the differences in Mach number are also plotted on the same figure. Both differences are small. Regarding density, the difference in solutions leads to an asymmetry between the low and the high field side, which is visible around the separatrix, down to the X-point legs, and around the inner magnetic surface, corresponding to the inner boundary in the simulation with hole. This asymmetry of density is associated to a very weak rotation of the plasma, both in the inner (negative) and in the private (positive) region. These differences are likely related to differences in particle fluxes through the inner boundary between the two solutions: the

ACCEPTED MANUSCRIPT

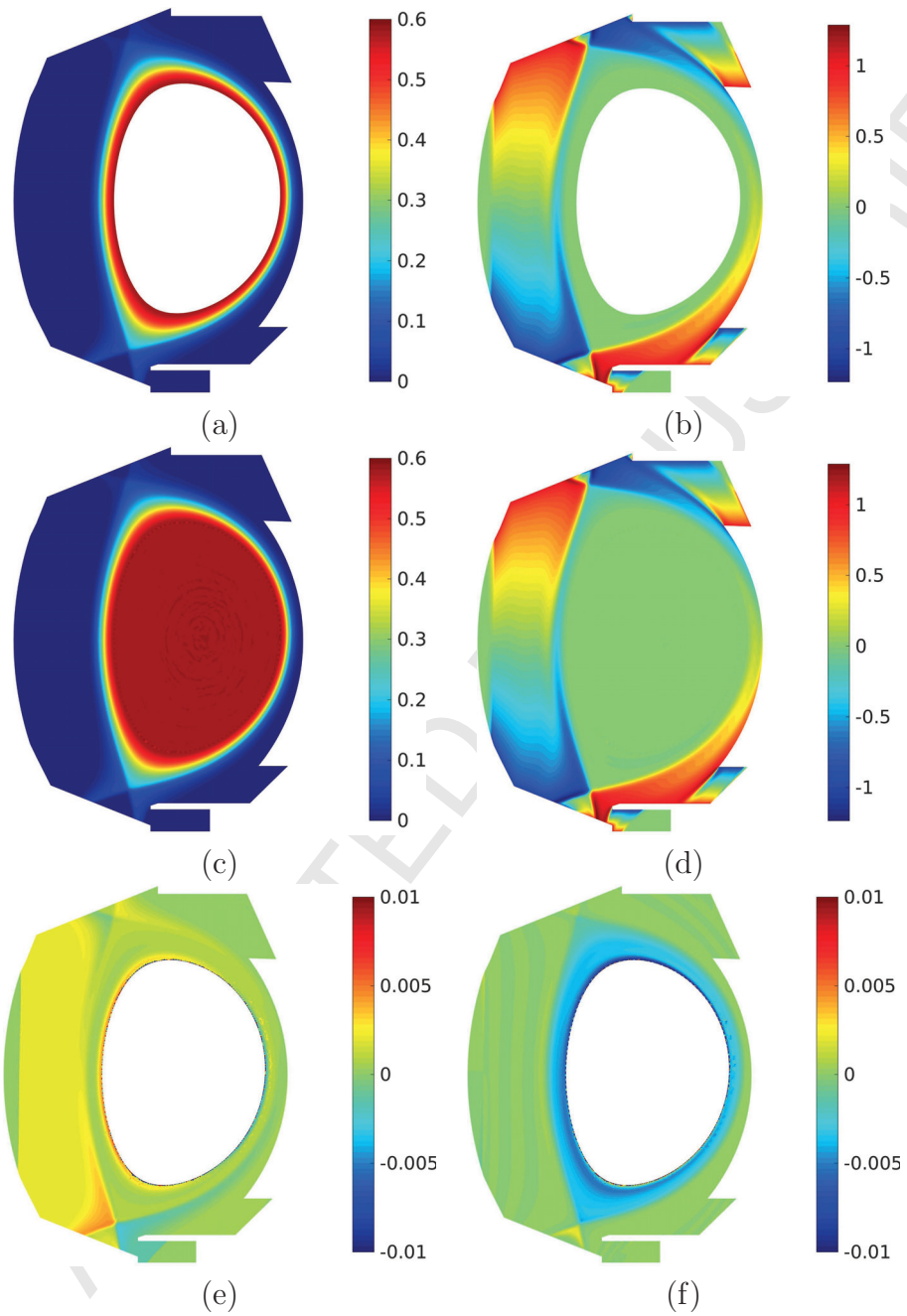

Figure 15: Maps of density n (a, c) and parallel Mach number $M_{\|}$ (b, d) at D=μ=0.038 ($= 1m^2s^{-1}$), background temperature $T_{bc} = 200eV$ and magnetic field magnitude at the axis $B_a = 3.6$Tesla. Solutions with drift in the WEST geometry. Relative differences for n (e) and differences for $M_{\|}$ (f) (bounded between -0.01 and 0.01).

ACCEPTED MANUSCRIPT

use of homogeneous Neumann conditions do not allow matching of particle flux through the boundary in both simulations.

7. Concluding remarks

A new discontinuous Galerkin solver has been presented for solving a 2D reduced model derived from fluid transport equations in the plasma edge of a tokamak, including both open and closed magnetic field lines. This reduced model for the ion density and the parallel momentum, contains however most of the numerical issues met in more complete fluid edge models, i.e. the magnetic geometry complexity, the strong anisotropy between the two magnetic field line directions, as well as the wall description through Bohm boundary conditions.

The present method uses high-order numerical schemes which guarantees the accuracy of the solutions by limiting numerical diffusion. Verification tests based on a manufactured solution have indeed shown the expected $p+1$ and exponential rates of convergence during the h-refinement and the p-refinement tests, respectively.

Associated to a finite-element discretization based on an unstructured mesh not aligned on the magnetic field, this method also allows to accurately discretize any realistic tokamak chamber as well as any magnetic geometry. It offers in this sense a flexibility never reached by any current codes used in the edge plasma physics community. The algorithm has been thus successfully benchmarked against the solution of the well-referenced transport code SOLEDGE2D-EIRENE in a realistic geometry of the WEST tokamak. The method, based on a mesh not aligned with the magnetic field lines, has been challenged by computing low perpendicular diffusion solutions. This is made possible by the low numerical diffusion of the method. The SOL width reduction with diffusion favorably compares to the prediction provided by the heuristic model of Goldston [41]. Finally, preliminary computations have been performed up to the tokamak cross-section center (WEST), showing a great flexibility of the solver on the magnetic geometry.

These validation tests show the capacity of the solver to deal with solutions computed in realistic geometries, involving supersonic flows, and possibly low physical perpendicular diffusion.

This paper shows that HDG could be an attractive method in a close future to solve fluid conservation equations for fusion, by offering new capacities to the new generation of codes that will be used for fusion operation.

ACCEPTED MANUSCRIPT

Acknowledgements This work was granted access to the HPC resources of IDRIS under the allocation i2017056912 and i20170242 made by GENCI, and of Aix-Marseille University, financed by the project (ANR-10-EQPX-29-01). The project leading to this publication has received funding from Excellence Initiative of Aix-Marseille University-A*MIDEX, a French "Investissements d'Avenir programme". This work was supported by the Energy oriented Centre of Excellence (EoCoE), grant agreement number 676629, funded within the Horizon2020 framework of the European Union.

ACCEPTED MANUSCRIPT

ACCEPTED MANUSCRIPT

References

[1] H. Bufferand, B. Bensiali, J. Bucalossi, G. Ciraolo, P. Genesio, P. Ghendrih, Y. Marandet, A. Paredes, F. Schwander, E. Serre, P. Tamain, Near wall plasma simulation using penalization technique with the transport code SOLEDG2D-EIRENE, J. Nucl. Mat. 84 (2013) 445–448.

[2] H. Bufferand, G. Ciraolo, Y. Marandet, J. Bucalossi, P. Ghendrih, J. Gunn, N. Mellet, P. Tamain, R. Leybros, N. Fedorczak, F. Schwander, E. Serre, Numerical modeling for divertor design of the WEST device with a focus on plasma wall interactions, Nucl. Fusion 55(5) (2015) 053025.

[3] P. Stangeby, The plasma boundary of magnetic fusion devices, IOP, 2000.

[4] T. Rognlien, Understanding of edge plasmas in magnetic fusion energy devices, Plasma Phys. Control. Fusion 47 (2005) 283–295.

[5] B. Scott, Free energy conservation in local gyrofluid models, Phys. Plasmas 12 (2005) 102307.

[6] C. Chang, S. Ku, Particle Simulation of Neoclassical Transport in the Plasma Edge, Contributions to Plasma Physics 46 (7-9) (2006) 496–503, ISSN 1521-3986.

[7] C. S. Chang, S. Ku, G. R. Tynan, R. Hager, R. M. Churchill, I. Cziegler, M. Greenwald, A. Hubbard, J. Hughes, Fast Low-to-High Confinement Mode Bifurcation Dynamics in a Tokamak Edge Plasma Gyrokinetic Simulation, Phys. Rev. Lett. 118 (2017) 175001.

[8] S. Braginskii, Transport processes in a plasma, Reviews in Plasma Physics 1 (1965) 205–311.

[9] A. N. Simakov, P. Catto, Drift-ordered equations for modelling collisional edge plasma, Contr. Plasma Phys. 44(1-3) (2004) 83–94.

[10] P. Tamain, H. Bufferand, G. Ciraolo, C. Colin, D. Galassi, P. Ghendrih, F. Schwander, E. Serre, The TOKAM3X code for edge turbulence fluid simulations of tokamak plasmas in versatile magnetic geometries, J. Comp. Phys. 321 (2016) 606–623.

ACCEPTED MANUSCRIPT

[11] D. Reiter, M. Baelmans, P. Börner, The EIRENE and B2-EIRENE Codes, Fusion Sci. Technol. 47(2) (2005) 172–186.

[12] X. Feng, O. Karakashian, Y. Xing, Recent developements in discontinous Galerkin finite element methods for partial differential equations, vol. 157, Springer, 2013.

[13] B. Cockburn, J. Gopalakrishnan, R. Lazarov, Unified hybridization of discontinuous Galerkin, mixed, and continuous Galerkin methods for second-order elliptic problems, SIAM J. Numer. Anal. 47(2) (2009) 1319–1365.

[14] B. Cockburn, B. Dong, J. Guzmán, A superconvergent LDG-hybridizable Galerkin method for second-order elliptic problems, Math. Comp. 77(264) (2008) 1887–1916.

[15] N. C. Nguyen, J. Peraire, B. Cockburn, An implicit high-order hybridizable discontinuous Galerkin method for linear convection-diffusion equations, J. Comput. Phys. 228(9) (2009) 3232–3254.

[16] N. C. Nguyen, J. Peraire, B. Cockburn, An implicit high-order hybridizable discontinuous Galerkin method for nonlinear convection-diffusion equations, J. Comput. Phys. 228(23) (2009) 8841–8855.

[17] N. C. Nguyen, J. Peraire, B. Cockburn, A hybridizable discontinuous Galerkin method for Stokes flow, Comput. Methods Appl. Mech. Eng. 199(2) (2010) 582–597.

[18] N. C. Nguyen, J. Peraire, B. Cockburn, An implicit high-order hybridizable discontinuous Galerkin method for the incompressible Navier-Stokes equations, J. Comput. Phys. 230(4) (2011) 1147–1170.

[19] B. Cockburn, J. Gopalakrishnan, N. C. Nguyen, J. Peraire, F.-J. Sayas, Analysis of HDG methods for Stokes flow, Math. Comp. 80(274) (2011) 723–760.

[20] G. Giorgiani, S. Fernández-Méndez, A. Huerta, Hybridizable discontinuous Galerkin with degree adaptivity for the incompressible Navier-Stokes equations, Comput. Fluids 98 (2014) 196–208.

ACCEPTED MANUSCRIPT

[21] Y. Chen, B. Cockburn, Analysis of variable-degree HDG methods for convection-diffusion equations. part I: Semimatching nonconforming meshes, IMA J. Numer. Anal. 32(4) (2012) 1267–1293.

[22] Y. Chen, B. Cockburn, Analysis of variable-degree HDG methods for convection-diffusion equations. part II: Semimatching nonconforming meshes, Math. Comp. 83 (2014) 87–111.

[23] M. Kronbichlery, W. A. Wally, A performance comparison of continuous and discontinuous Galerkin methods with fast multigrid solvers, arXiv preprint.

[24] R. Heath, I. Famba, P. Morrison, C. Michler, A discontinuous Galerkin method for the Vlasov-Poisson system, J. Comp. Phys. 231(4) (2012) 1140–1174.

[25] U. Shumlak, R. Lilly, N. Reddell, B. Sousa, B. Srinivasan, Advanced physics calculations using a multi-fluid plasma model, Comp. Phys. Comm. 182(9) (2011) 1767–1770.

[26] C. Michoski, D. Meyerson, T. Isaac, F. Waelbroeck, Discontinuous Galerking methods for plasma physics in the scape-off layer of tokamaks, J. Comp. Phys. 274 (2014) 898–919.

[27] J. Bucalossi, *et al.*, The WEST project: Testing ITER divertor high heat flux component technology in a steady state tokamak environment, Fusion Eng.& Design 89(7-8) (2014) 907–912.

[28] P. Tamain, P. Ghendrih, E. Tsitrone, V. Grandgirard, X. Garbet, Y. Sarazin, E. Serre, G. Ciraolo, G. Chiavassa, TOKAM-3D: A 3D fluid code for transport and turbulence in the edge plasma of Tokamaks, J. Comp. Phys. 229 (2009) 361–378.

[29] J. Loizu, P. Ricci, F. Halpern, S. Jolliet, Boundary conditions for plasma fluid models at the magnetic presheath entrance, Phys. of Plasma 19 (2012) 122307.

[30] A. Montlaur, S. Fernández-Méndez, A. Huerta, Discontinuous Galerkin methods for the Stokes equations using divergence-free approximations, Int. J. Numer. Methods Fluids 57(9) (2008) 1071–1092.

ACCEPTED MANUSCRIPT

[31] M. A. Taylor, B. A. Wingate, R. E. Vincent, An algorithm for computing Fekete points in the triangle, SIAM J. Numer. Anal. 38 (2000) 1707–1720.

[32] P. Angot, T. Auphan, O. Gués, An optimal penalty method for a hyperbolic system modeling the edge plasma transport in a tokamak, J. Comp. Phys. 261 (2014) 1–22.

[33] C. Shu, S. Osher, Efficient implementation of essentially nonoscillatory shock-capturing schemes. II, J. Comp. Phys. 83(1) (1989) 32–78.

[34] A. Kanevsky, M. Carpenter, J.S.Hesthaven, Idempotent filtering in spectral and spectral element methods, J. Comp. Phys. 220(1) (2006) 41–58.

[35] E. Tadmor, Shock capturing by the spectral viscosity method, Comput. Methods Appl. Mech. Engrg. 80(1-3) (1990) 197–208.

[36] A. Gelb, S. Gottlieb, Advances in The Gibbs Phenomenon with Detailed Introduction. Chapter 7: The Resolution of the Gibbs Phenomenon for Fourier Spectral Methods, Abdul J. Jerri, Editor, Sampling Publishing, Potsdam, New York, 2007.

[37] J. Guermond, R. Pasquetti, B. Popov, Entropy viscosity method for nonlinear conservation laws, J. Comp. Phys. 230(11) (2011) 4248–4267.

[38] P. Persson, J. Peraire, Sub-cell shock capturing for discontinuous Galerkin methods, In proc. 44th AIAA meeting (2006) https://doi.org/10.2514/6.2006–112.

[39] S. Wandzurat, H. Xiao, Symmetric quadrature rules on a triangle, Comp. & Math. with Applications 45(12) (2003) 1829–1840.

[40] J. Donea, A. Huerta, Finite element methods for flow problems, F, John Wiley & Sons, Chichester (UK), 2003.

[41] R. Goldston, Heuristic drift-based model of the power scrape-off width in low-gas-puff H-mode tokamak, Nucl. fusion 52 (2012) 013009.

[42] A. Paredes, H. Bufferand, G. Ciraolo, F. Schwander, E. Serre, P. Ghendrih, P. Tamain, A penalization technique to model plasma facing components in a tokamak with temperature variations, J. Comp. Phys. 274 (2014) 283–298.

ACCEPTED MANUSCRIPT

[43] P. Ghendrih, K. Bodi, H. Bufferand, G. Chiavassa, G. Ciraolo, N. Fedorczak, L. Isoardi, A. Paredes, Y. Sarazin, E. Serre, F. Schwander, P. Tamain, Transition to supersonic flows in the edge plasma, Plasma Phys. Control. Fusion 53(5) (2011) 054019.

[44] H. Bufferand, G. Ciraolo, P. Ghendrih, P. Tamain, F. Schwander, E. Serre, Y. Marandet, Study of transition to supersonic regime in divertor SOL using SOLEDGE2D code, Plasma Phys. Control. Fusion 54(4-6) (2014) 378–382.

[45] C. Colin, P. Tamain, F. Schwander, E. Serre, H. Bufferand, G. Ciraolo, N. Fedorczak, P. Ghendrih, Impact of the plasma-wall contact position on edge turbulent transport and poloidal asymmetries in 3D global turbulence simulations, J. Nucl. Mat. 463 (2015) 654–658.

[46] D. Reiser, T. Eich, Drift-based scrape-off particle width in X-point geometry, Nucl. Fusion 57(4) (2017) 046011.

ACCEPTED MANUSCRIPT